Large Signal Field Analysis of a Linear Beam Traveling Wave Amplifier for a Sheath-helix Model of the Slow-wave Structure Supported by Dielectric Rods. Part 2: Numerical Results

Natarajan Kalyanasundaram* and Amita Agnihotri

Abstract—Numerical computation of induced surface current density, power gain, conversion efficiency, optimum interaction length and harmonic generation etc. pertaining to large-signal operation of a linear beam travelling wave tube amplifier (TWTA) employing a dielectric-loaded sheath helix model for the slow-wave structure based on the large-signal theory developed in Part 1 of this paper is presented, and comparison with the results of other large-signal theories and available experimental evidence is made.

1. INTRODUCTION

In Part 1 of this paper, a rigorous method of analysing the large-signal behaviour of a linear beam traveling wave tube amplifier (TWTA) with the slow-wave structure modeled by a dielectric-loaded sheath helix was presented starting from the governing equations of classical electrodynamics. A key step in the analysis was an expansion of the steady-state beam current density in a Fourier-series in the time variable and a representation of the 'Fourier coefficients' as nonlinear functionals of the electron arrival time through a Green's function sequence for the slow-wave structure. With a view to identifying the form of the Green's functions, the field components were also expanded in Fourier series in the time variable, the Fourier coefficients being now functions only of the spatial co-ordinates. Substituting the Fourier-series expansions for the field components and the beam-current density into Maxwell's equations and solving the resulting nonhomogeneous boundary value problem with the help of a second Fourier-series expansion in the axial coordinate, the Green's functions for the slow-wave structure were determined. Using the Green's function representation of the axial electric field component inside the beam as a nonlinear functional of the electron arrival time, the problem was reduced to one of solving for the electron arrival time as the fixed point of a nonlinear (integral) operator equation in a function space by the method of successive approximations.

The numerical computation of the TWTA characteristics to be taken up in this part will be based on the above double Fourier-series representation (in the time variable and the axial coordinate) of the particular solution for the axial electric and magnetic field components truncated at the third temporal harmonic (i.e., $m \leq M = 3$) and the 64th spatial harmonic (i.e., $|n| \leq N = 64$). The computations are carried out for an operating frequency f_0 of 6 GHz and the dimensionless interaction length d varying between 120 and 160 in steps of 2. For the above choices of the operating frequency and the interaction length, the resonance condition is not even approximately satisfied by any of integer pairs (m, n) with $1 \leq m \leq 3$ and $\lfloor ma_1/k_d \rfloor + 1 \leq n \leq 64$, where for any real number $X, \lfloor X \rfloor$ denotes its integer part. Hence the need for using the alternate expressions for the particular solution developed in Appendix B of Part 1 does not arise. The equations of this part will be numbered consecutively from those of Part 1 and also the notation of Part 1 will be employed.

2. ELECTRON ARRIVAL TIME, EXIT SPEED AND AXIAL ELECTRIC FIELD

The truncated double Fourier series for the axial electric field component can be written from (41) in a form suitable for numerical work as

$$\mathcal{E}_1(z,r,t) = \sum_{m=1}^{M} [E_{1m}(z,r)\exp(jmt) + c.c.] \tag{46a}$$

$$E_{1m}(z,r) = \delta_{1m}AI_0(\tau_1 r)\exp(-j\beta_1 z)/2I_0(\tau_1) + (q_0/\pi a_1 d)[F_{sm}(z,r) + jF_{cm}(z,r)]/2m$$
$$m = 1, 2, 3 \ldots, M \tag{46b}$$

$$F_{lm}(z,r) = \sum_{n=0}^{N}(2-\delta_{n0})[F_{lmn}(r)\cos(nk_d z) - F_{lmn}(1)W_m(r)\cos(\beta_m z)]$$
$$l = s, c \tag{46c}$$

$$F_{lmn}(r) = \int_0^a G_{mn}(r,y)f_{lmn}(y)ydy \quad l = s, c \tag{46d}$$

$$f_{smn}(y) = \int_0^d \cos(nk_d x)dx \int_{-\pi}^{\pi} \sin\ mt(x,y,\tau)d\tau \tag{46e}$$

$$f_{cmn}(y) = \int_0^d \cos(nk_d x)dx \int_{-\pi}^{\pi} \cos\ mt(x,y,\tau)d\tau \tag{46f}$$

where the electron arrival time $t(z,r,t_0)$, of course, satisfies the nonlinear integral Equation (43).

The following (constant) values of input-signal parameters and beam parameters will be used in the numerical computation of the TWTA characteristics.

The (unique) roots of the dielectric-loaded sheath-helix dispersion Equation (29) re-expressed in the form

$$\tau_m I_0(\tau_m)/I_1(\tau_m) + \tilde{\tau}_m \Delta_{m10}(1)/\Delta_{m11}(1) = (ma_1 \cot\psi/a_2)^2 (I_1(\tau_m)/\tau_m I_0(\tau_m) + \varepsilon_{eff}\Delta_{m01}(1)/\tilde{\tau}_m\Delta_{m00}(1))$$

for the renormalized propagation phase constants $\beta_{ma} \underline{\underline{\Delta}} \beta_m/a_2$, $m = 1,2,3$, are $\beta_{1a} = 9.3098$, $\beta_{2a} = 18.56305$, $\beta_{3a} = 27.80771$, where $k_{0a}\underline{\underline{\Delta}}a_1/a_2 = \omega_0\bar{a}/c$ and the simpler expressions for τ_m and $\tilde{\tau}_m$ in terms of β_{ma} and k_{0a} are

$$\tau_m^2(r) = (\beta_{ma}^2 - m^2 k_{0a}^2)^{1/2} \ \text{and} \ \tilde{\tau}_m(r) = (\beta_{ma}^2 - m^2 k_{0a}^2\varepsilon_{eff})^{1/2}$$

For the choice $a_1 = v_0/c = v_p/c = k_{0a}/\beta_{1a} = 0.135055$, that ensures perfect synchronism between the electron beam and the traveling electromagnetic wave at the input plane, the corresponding values of a_2 and β_m, $m = 1,2,3$, are $a_2 = 0.107422$, $\beta_1 = 1.00$, $\beta_2 = 1.99408$, $\beta_3 = 2.98716$. We observe that $\beta_m < m\beta_1$, $m = 1,2,3$, attesting to the dispersive nature of the slow waves supported by a dielectric-loaded sheath-helix. Neglecting the relativistic variation of electron mass with speed, the value of the anode voltage required to accelerate the electrons (emitted from the cathode with zero initial speed) to an axial speed of $v_0 = 0.135055c$ works out to be $V_0 = 4.66\,\text{kV}$.

A parameter α, defined by

$$\alpha \underline{\underline{\Delta}} 10\log_{10}(P_{in}/P_{dc}) \tag{47}$$

will now be introduced for describing the numerical results of this paper. In the above definition

$$P_{in} = \pi A_0^2\bar{a}^2 Y_0 P_{11} \tag{48}$$

is the input-signal power (assuming it to be that due to a forward-propagating cold wave at the input-signal frequency) and $P_{dc} = V_0I_0$ is the 'dc' power of the beam. The expression for the non-dimensional

quantity P_{11} appearing in (48) is

$$P_{11} = (1/2) \begin{bmatrix} (\beta_1 a_1/\tau_1^2 a_2^2)\{I_1^2(\tau_1)/I_0^2(\tau_1) + 2I_1(\tau_1)/\tau_1 I_0(\tau_1) - 1\} - (\beta_1 \tan\psi/a_1)\{I_0^2(\tau_1)/I_1^2(\tau_1) \\ -2I_0(\tau_1)/\tau_1 I_1(\tau_1) - 1\} + (\beta_1 a_1 \varepsilon_{eff}/\tilde{\tau}_1^2 a_2^2)\{1 + 2\Delta_{101}(1)/\tilde{\tau}_1\Delta_{100}(1) \\ -(\Delta_{101}(1)/\Delta_{100}(1))^2 + \tilde{\tau}_1^{-2}\Delta_{100}^{-2}(1)\} - (\beta_1 \tan^2\psi/a_1)\{1 - 2\Delta_{110}(1)/\tilde{\tau}_1\Delta_{111}(1) \\ -(\Delta_{110}(1)/\Delta_{100}(1))^2 + \tilde{\tau}_1^{-2}\Delta_{111}^{-2}(1)\} \end{bmatrix} \quad (49)$$

For the parameter values of Table 1 and the truncation orders of $M = 3$ and $N = 64$, the nonlinear integral Equation (43) is iteratively solved on a PC for the electron arrival time $t(z, r, t_0)$ making use of the representation (46) for the axial electric field component inside the beam, and the results showing the behaviour of the arrival time $t(d, r, t_0)$ of electrons at the output plane and the exit electron speed

$$v(d, r, t_0) = 1/t_z(d, r, t_0) = \left\{1 - 2\varepsilon \int_0^d \mathcal{E}_1(s, r, t(s, r, t_0))ds\right\}^{1/2}$$

as functions of the entrance time t_0 are plotted in Figs. 1(a) and 2(a) for $r = 0$ (beam axis) and in Figs. 1(b) and 2(b) for $r = a$ (beam boundary) for the values of $d = 120$ and $\alpha = -50\,\text{dB}, -40\,\text{dB}, -30\,\text{dB}$ and $-20\,\text{dB}$.

It is observed from Fig. 1 that $t(z, r, t_0)$ is a monotonically increasing function of t_0 for $\alpha = -50\,\text{dB}$, but not so for $\alpha = -40\,\text{dB}, -30\,\text{dB}$ and $-20\,\text{dB}$. This observation is in conformity with the well-known fact that electron overtaking is the rule if the input-signal power is sufficiently large. It is also seen from Fig. 1 that electrons entering the interaction region over a period of the input signal undergo a net

Table 1. Parameter values of the TWTA.

Description	Notation	Numerical value
Operating frequency	$f_0 = \omega_0/2\pi$	6 GHz
Input-signal phase factor	$A = e^{j\theta}$	1
Sheath-helix pitch angle	Ψ	10°
Sheath-helix radius	$\bar{a}$	1 cm
Outer-conductor radius	$\bar{b}$	2.24 cm
Effective dielectric constant of support rods	ε_{eff}	2.25
Beam current	I_0	60 mA
Beam radius	$\bar{a}_0$	0.5 cm
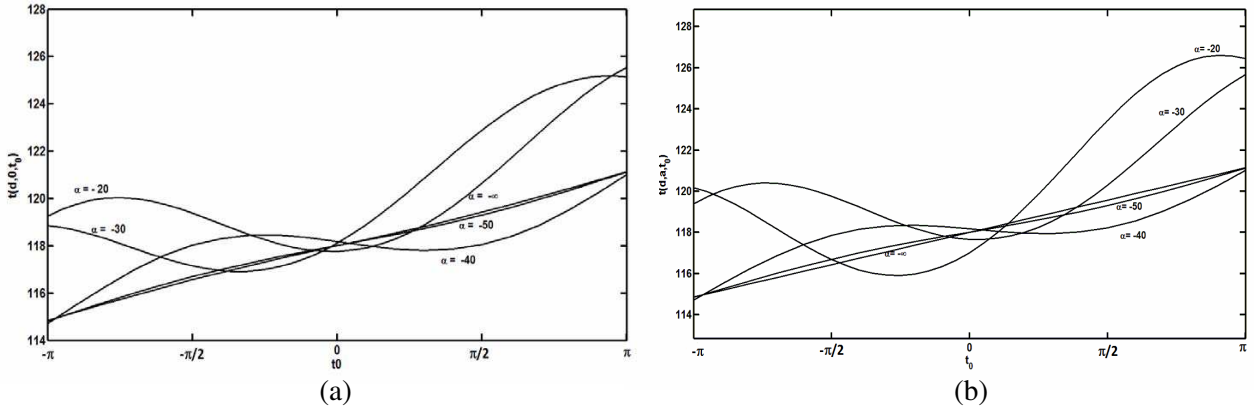
Figure 1. (a) Variation of electron arrival time with entrance time t_0, for $r = 0$ and $d = 120$. (b) Variation of electron arrival time with entrance time t_0, for $r = a$ and $d = 120$.

retardation or acceleration to varying amounts, relative to their unperturbed trajectories, depending on their entrance time, their radial position and input-signal level. The relative number of electrons in the retarded category and the maximum phase lag $(\underline{\underline{\triangle}} \max_{-\pi \leq t_0 < \pi} \theta(d, r, t_0))$ are seen in general, to increase with the input-signal level. Here $\theta(d, r, t_0) \underline{\underline{\triangle}} t(d, r, t_0) - t_0$ is the dimensionless transit time.

It may be observed from the plots of exit electron speed in Figs. 2(a) and 2(b) that both the negative
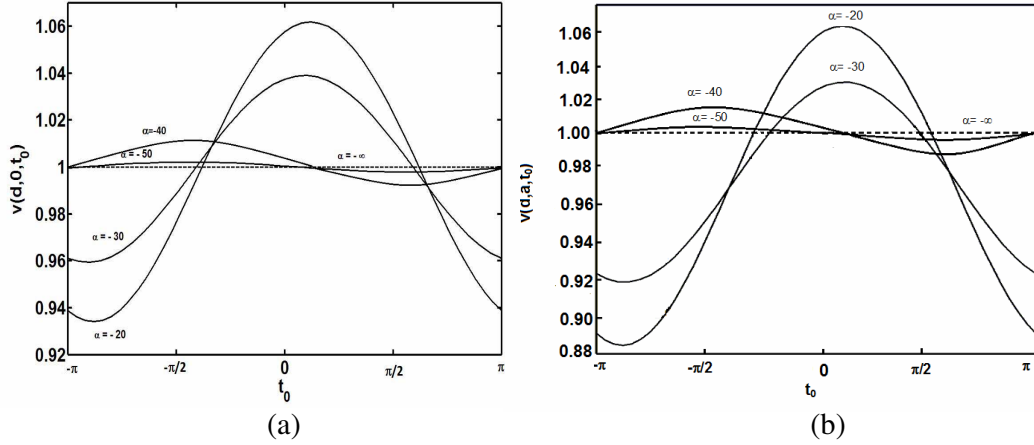
Figure 2. (a) Variation of dimensionless exit electron speed with entrance time for $r = 0$ and $d = 120$. (b) Variation of dimesionless exit electron speed with entrance time for $r = a$ and $d = 120$.
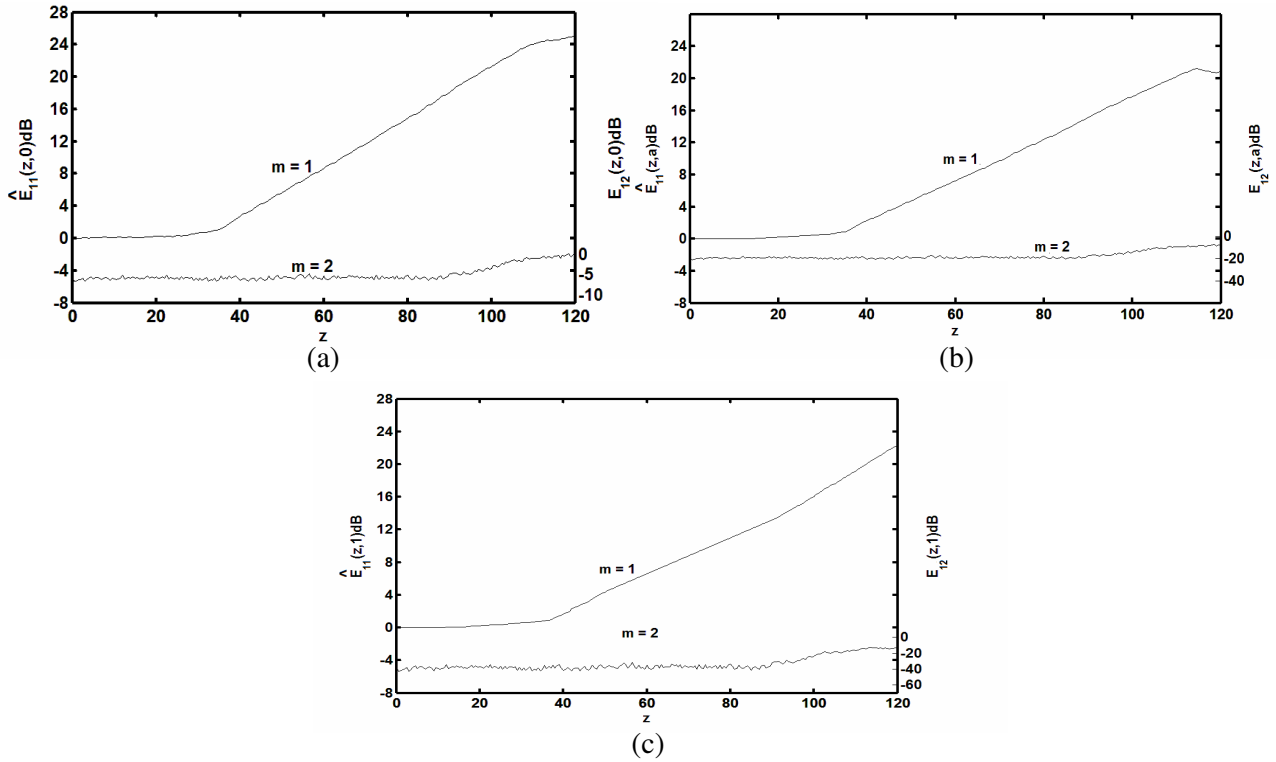
Figure 3. (a) Build-up of fundamental and second harmonic components of axial electric field with distance along the axis for $r = 0$, $\alpha = -20\,\text{dB}$ and $d = 120$. (b) Build-up of fundamental and second harmonic components of axial electric field with distance along the axis for $r = a$, $\alpha = -20\,\text{dB}$ and $d = 120$. (c) Build-up of fundamental and second harmonic components of axial electric field with distance along the axis for $r = 1$, $\alpha = -20\,\text{dB}$ and $d = 120$.

as well as the positive deviation of the exit electron speed from the entrance electron speed over a period of the input signal increases with input-signal level, the negative deviation tending to dominate over the positive deviation with an increase in the input signal level. Moreover, the perturbation of the exit electron speed from the entrance speed tends to be larger for the peripheral electrons than for the axial electrons.

Graphs showing the build-up of the first two harmonics of the axial electric field component as given by the normalized Fourier-coefficient magnitudes $\hat{E}_{1m}(z,r) \underline{\Delta} |E_{1m}(z,r)/E_{11}(0,r)|$, $m = 1$, 2, are plotted in Fig. 3 for the parameter values $d = 120$, $\alpha = -20\,\text{dB}$, and $r = 0$ (beam axis), a (beam boundary) and 1 (helix boundary).

It is seen from Fig. 3 that the second harmonic field is smaller by at least two orders of magnitude than the fundamental field all through the interaction region. A comparison of the three curves of Fig. 3, for $m = 1$, also reveals that the strongest interaction between the electron beam and the electromagnetic field takes place near the beam axis; the interaction becomes the weakest at the beam boundary and grows once again progressively stronger as the helix boundary is approached. Radial variation of the normalized fundamental axial electric field component $\tilde{E}_{11}(z,r) \underline{\Delta} |E_{11}(z,r)/E_{11}(z,1)|$ at the planes $z = 0$, $d/2$ and d for the same parameter values are plotted in Fig. 4. It is clear from the figure that the radial variation of the axial electric field component is not affected to any significant extent by the axial position at which the field is evaluated.

3. INDUCED CURRENT DENSITY

The density of the surface current flowing along the sheath helix may be evaluated using the boundary condition on the tangential component of the magnetic field across a discontinuity. This condition together with the fourth of sheath-helix boundary conditions (19a) enables the mth ($m = 1, 2, 3$) Fourier-coefficient $J_{sm}(z)$ of the surface current density component along the direction of infinite conductivity on the sheath helix normalized with respect to its value at $z = 0$ to be expressed as

$$J_{sm}(z) = [H_{1m}(z,1-) - H_{1m}(z,1+)]/[H_{11}(0,1-) - H_{11}(0,1+)] \tag{50}$$

From (24b), (38b), (31b), (33), (35b) and (39), the discontinuity in $H_{1m}(z,r)$ at the helix boundary may be estimated to be

$$H_{1m}(z,1-) - H_{1m}(z,1+) = (-ja_2 \tan\psi/2a_1)\delta_{1m}\left[\tau_1 I_0(\tau_1)/I_1(\tau_1) + \tilde{\tau}_1\Delta_{110}(1)/\Delta_{111}(1)\right]\exp(-j\beta_1 z)$$

$$+ \left(q_0 a_2 \tan\psi/2\pi m^2 a_1^2 d\right)\left\{\sum_{n=0}^{N}(2-\delta_{0n})\{p_{mn}C_0(p_{mn})/C_1(p_{mn}) + \tilde{p}_{mn}\Delta_{mn10}/\Delta_{mn11}\}(h_{cmn}-jh_{smn})\cos(nk_d z)\right.$$

$$\left. -\{\tau_m I_0(\tau_m)/I_1(\tau_m) + \tilde{\tau}_m\Delta_{m10}(1)/\Delta_{m11}(1)\}\cos(\beta_m z)\left(\sum_{n=0}^{N}(2-\delta_{0n})(h_{cmn}-jh_{smn})\right)\right\} \tag{51}$$
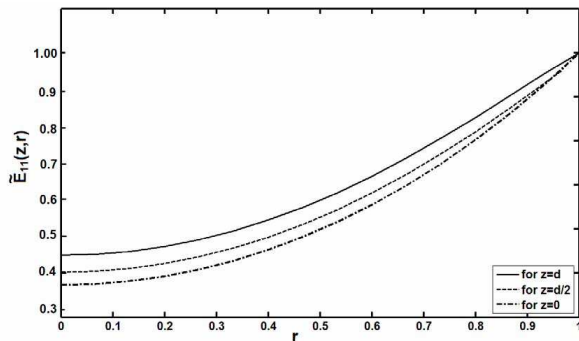
Figure 4. Radial variation of axial electric field component for $d = 120$ and $\alpha = -20\,\text{dB}$.
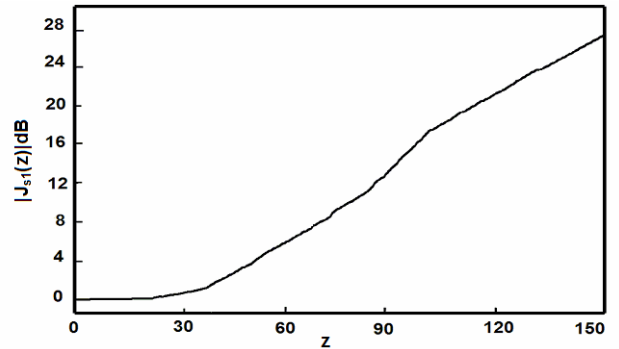
Figure 5. Variation of fundamental surface current density magnitude with axial distance for $\alpha = -20\,\text{dB}$ and $d = 150$.

where

$$h_{imn}(r) \underline{\underline{\Delta}} \Lambda_{mn}^{-1} \int\limits_0^a \left(C_0(p_{mn}y)/C_0(p_{mn}) \right) f_{imn}(y)ydy, \quad i = c, s$$

the functions $C_0(.)$ and $C_1(.)$ are defined in (36) and we have set input-signal phase factor $A = e^{j\theta} = e^{j0} = 1$. Thus the computation of the surface current density induced on the slow wave structure is seen to be quite straightforward.

The variation in magnitude of the surface-current density $J_{s1}(z)$ with axial distance z is plotted in Fig. 5 for $d = 150$ and $\alpha = -20\,$dB. The near-exponential build-up of the surface-current density with interaction distance can be easily made out from Fig. 6 which shows the behaviour of $\mathrm{Re}J_{s1}(z)$ with z for the same values of d and α. Fig. 6 also puts into evidence the traveling nature of the interaction between the electron beam and the electromagnetic field since $\mathrm{Re}J_{s1}(z)$ represents a snapshot of the surface current density wave $|J_{s1}(z)|\cos(t - \theta_{s1}(z))$ evaluated at time $t = 0$ where $\tan(\theta_{s1}(z)) = \mathrm{Im}J_{s1}(z)/\mathrm{Re}J_{s1}(z)$.
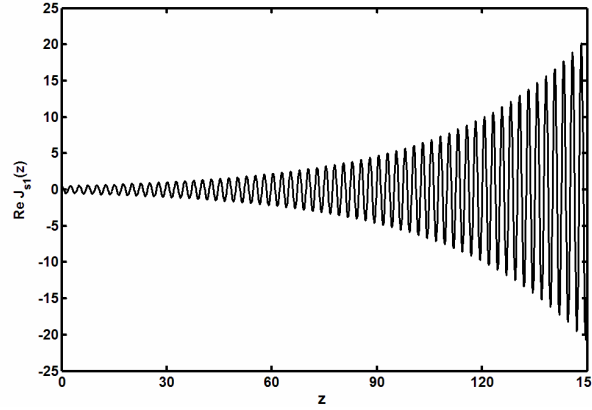
Figure 6. Variation of real part of the fundamental component of induced current density with axial distance for $\alpha = -20\,$dB and $d = 150$.

4. POWER GAIN AND CONVERSION EFFICIENCY

With a view to formulating suitable definitions for these two parameters, consider a coaxial cylinder of radius b with end faces S_i and S_o at the input and the output planes of the helix, and the lateral surface S_l at $r = b$ coincident with the inner surface of the outer perfectly conducting circular cylindrical shell. Taking the output power P_{out} to be the net (time-averaged) power flowing out through the output end face S_o of this cylinder (there will not be any power flow through the lateral surface S_l) and the input power P_{in} to be the net power flowing into the cylinder through the input end face S_i, the total power gain g_{tot} and the total conversion efficiency η_{tot} may be defined respectively as

$$g_{tot} \underline{\underline{\Delta}} P_{out}/P_{in} \quad \text{and} \quad \eta_{tot} \underline{\underline{\Delta}} (P_{out} - P_{in})/P_{dc} = (P_{out} - P_{in})/V_0 I_0$$

Applying the Poyinting theorem [1] to the volume bounded by $S_i \cup S_l \cup S_0$, it is seen that

$$P \underline{\underline{\Delta}} P_{out} - P_{in} = \sum_{m=1}^{\infty} 4\pi\,\bar{a}^2 A_0^2 Y_0 P_m$$

Here $Y_0 = 1/Z_0$ is the intrinsic admittance of free space and

$$P_m = -\mathrm{Re} \int_0^d \int_0^a E_{1m}(z,r)i_m^*(z,r)rdrdz$$

$$= -\delta_{1m}(q_0/2\pi d)\sin(\beta_1 d/2)\left[\sum_{n=0}^N (2-\delta_{0n})\left(\beta_1/\left(\beta_1^2 - n^2 k_d^2\right)\right)\right]$$

$$\times \int_0^a (\cos(\beta_1 d/2) f_{1nc}(r) + \sin(\beta_1 d/2) f_{1ns}(r)) \, (I_0(\tau_1 r)/I_0(\tau_1)) \, r dr \Bigg] + (q_0/2\pi d)^2 (\beta_m/ma_1) \sin(\beta_m d)$$

$$\times \left\{ \left(\sum_{n=0}^N (2 - \delta_{0n}) \lambda_{mns}/\Lambda_{mn} \right) \left(\sum_{n=0}^N (2 - \delta_{0n}) \mu_{mnc}/ \left(\beta_m^2 - n^2 k_d^2 \right) \right) \right.$$

$$\left. - \left(\sum_{n=0}^N (2 - \delta_{0n}) \lambda_{mnc}/\Lambda_{mn} \right) \left(\sum_{n=0}^N (2 - \delta_{0n}) \mu_{mns}/ \left(\beta_m^2 - n^2 k_d^2 \right) \right) \right\} \tag{52}$$

where

$$\lambda_{mni} \triangleq \int_0^a \left(C_0(p_{mn}y)/C_0(p_{mn}) \right) f_{mni}(y) y dy, \qquad i = c, \, s$$

$$\mu_{mni}(r) \triangleq \int_0^a \left(I_0(\tau_m y)/I_0(\tau_m) \right) f_{mni}(y) y dy, \qquad i = c, \, s$$
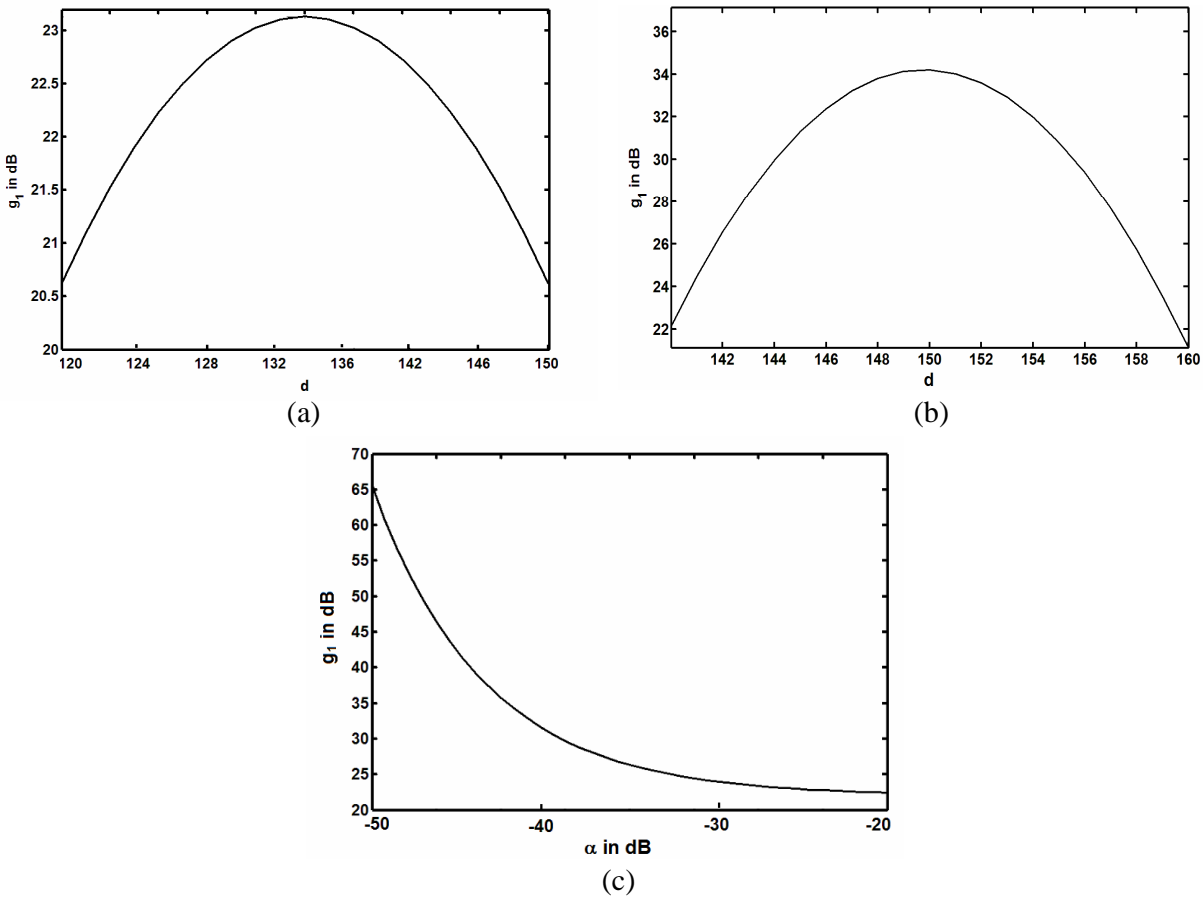
Figure 7. (a) Variation of fundamental power gain with normalized interaction length for $\alpha = -20$ dB. (b) Variation of fundamental power gain with normalized interaction length for $\alpha = -30$ dB. (c) Variation of power gain with input power for $\alpha = -20$ dB and $d = 135$.

and symmetry of the partial Green's function $G_{mn}(r, y)$, that is $G_{mn}(r, y) = G_{mn}(y, r)$ for $(r, y) \in [0, a] \times [0, 1]$, has been used to verify that there is no contribution from double integrals of the form

$$\int_0^a \int_0^a G_{mn}(r, y)[f_{mns}(r)f_{mnc}(y) - f_{mnc}(r)f_{mns}(y)]r dr dy$$

to P_m. From (48), the (fundamental) power gain g_1 can be expressed as

$$g_1 \underline{\underline{\triangle}} (4\pi \bar{a}^2 A_0^2 Y_0 P_1 + P_{in})/P_{in} = 1 + 4 P_1/P_{11} \tag{53}$$

where P_{11} is defined by (49). Similarly, the conversion efficiency for mth harmonic may be expressed as

$$\eta_m = (4\pi\bar{a}^2 A_0^2 Y_0 P_m/V_0 I_0) = (4 P_m/P_{11})10^{(2+0.1\alpha)}\%, \quad m = 1, 2, 3 \tag{54}$$

The variation of the fundamental power gain g_1 with the normalized interaction length d for $\alpha = -20\,\text{dB}$ and $\alpha = -30\,\text{dB}$ are shown in Figs. 7(a) and 7(b) respectively. It may be seen from these figures that the power gain attains flat maxima at about $d = 134$ for an input signal level of $\alpha = -20\,\text{dB}$ and at about $d = 150$ for $\alpha = -30\,\text{dB}$, the corresponding values of saturation gains being about $23\,\text{dB}$ and $34\,\text{dB}$ respectively. These observations lend credence to the anticipated behaviour of the optimum interaction length and the saturation power gain, namely, values of both parameters increase as the input-signal level is decreased. The variation of the fundamental power gain g_1 with input power level α for $d = 135$ is plotted in Fig. 7(c) which shows a monotonic decrease in power gain as the input-signal power is increased with the decay rate coming down from a large value near $\alpha = -50\,\text{dB}$ to a very small value near $\alpha = -20\,\text{dB}$.
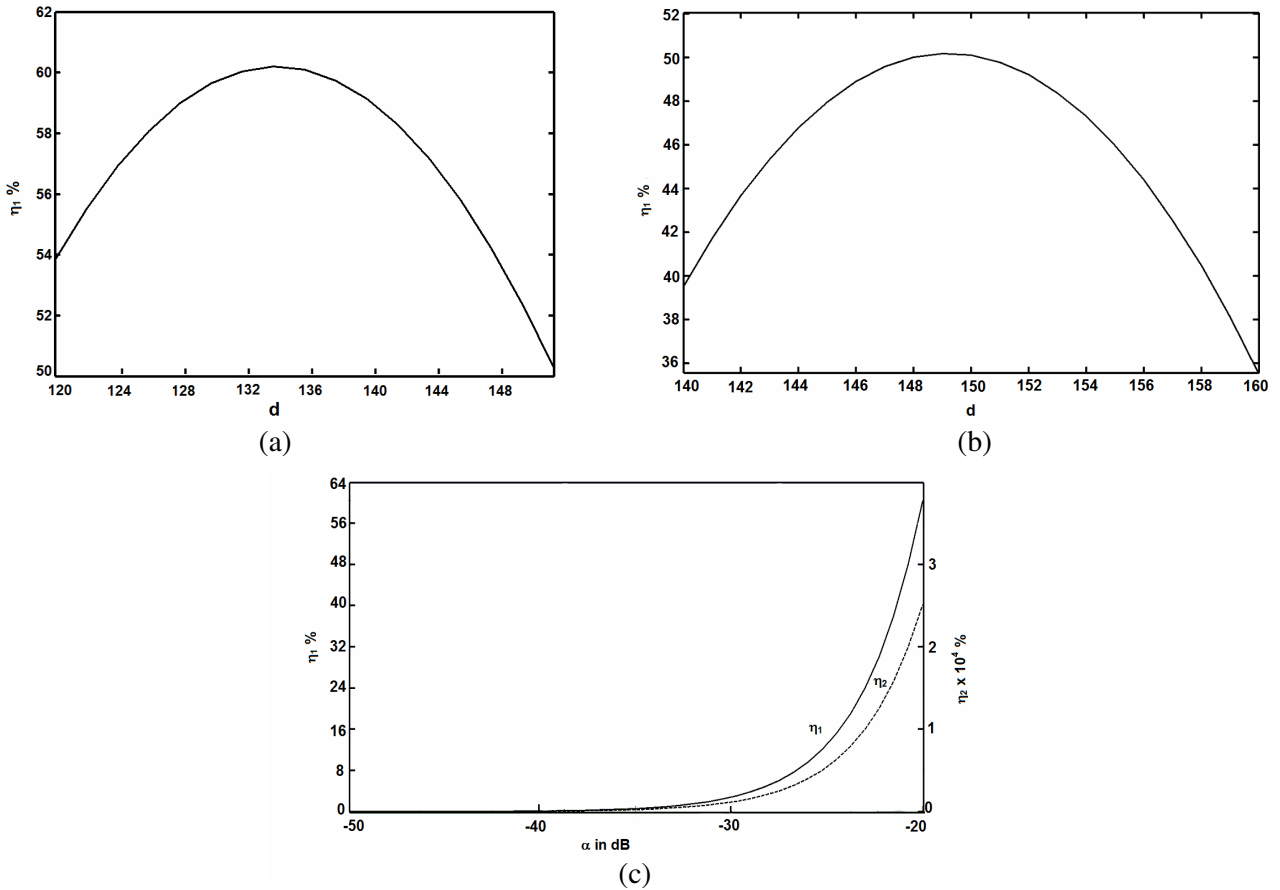
Figure 8. (a) Variation of fundamental conversion efficiency with normalized interaction length for $\alpha = -20\,\text{dB}$. (b) Variation of fundamental conversion efficiency with normalized interaction length for $\alpha = -30\,\text{dB}$. (c) Variation of fundamental and second harmonic conversion efficiency with input power for $d = 135$.

The variation of the fundamental conversion efficiency η_1 with normalized interaction length d for $\alpha = -20$ dB and $\alpha = -30$ dB is shown in Figs. 8(a) and 8(b) respectively. It may be seen from these plots that the fundamental conversion efficiency attains flat maxima at about $d = 134$ for an input signal level of $\alpha = -20$ dB and at about $d = 150$ for $\alpha = -30$ dB, the corresponding values of saturation efficiencies being about 60% and 50% respectively. It should come as no surprise that the optimal value of the interaction length at which power-gain curve as well as the efficiency-curve attains its maximum turn out to be identical for the same value of the input-signal level α. This is because the efficiency η_1 (as a percentage) and the power gain g_1 (in dB) are related by

$$\eta_1 = f(g_1, \alpha) = \left(10^{0.1\, g_1} - 1\right) 10^{(2+0.1\alpha)}$$

where f is seen to be a monotonically increasing function of g_1 for a fixed α.

The variations of the fundamental and the second harmonic conversion efficiencies η_1 and η_2 with α for $d = 135$ are shown in Fig. 8(c) (Note that η_2 is plotted in a scale which is magnified 10^4 times the scale for η_1). As expected, both η_1 and η_2 exhibit a near-exponential increase with respect to the input signal power; however, the second harmonic efficiency η_2 is at least four orders of magnitude smaller than the fundamental conversion efficiency η_1. In view of the fact that the contribution of the harmonics generated by the nonlinear electron-wave interaction in a linear beam TWTA to the output power is imperceptibly small, it is possible to retain only the component at the input-signal frequency in the temporal Fourier-series representation of the convection current density $i(z, r, t)$ and the electromagnetic field components $\mathcal{E}_k(z, r, t)$ and $\mathcal{H}_k(z, r, t)$, $k = 1, 2, 3$, without incurring any significant loss in accuracy.

5. CONCLUDING COMMENTS

An examination of the results presented in this paper in light of the results of the large-signal field theory of an open sheath helix [2, 3] and other large-signal non-field theories [4, 5] and available experimental evidence [6] lead to the following conclusions.

(i) The values of the saturation power gain and the conversion efficiency compare very favourably with those predicted by large-signal non-field theories [4, 5] and the experimentally observed values [6]. The unusually small values of these parameters obtained in [3] for the open sheath-helix model of the slow-wave structure may be attributed to the power loss due to the presence of 'radiating terms' (associated with Hankel functions in the Fourier-series representation of the particular solution for the field components valid in the unbounded region exterior to the open sheath helix).

(ii) There exists an optimum interaction length, which is a function of the parameter values and the input-signal level, for a linear beam TWTA as in the case of a klystron amplifier [7].

(iii) A linear beam TWTA is a very poor harmonic generator and consequently a very poor frequency converter even under large-signal conditions. Thus the harmonic distortion introduced by a linear beam TWTA with the slow-wave structure modeled by a dielectric-loaded sheath helix is negligibly small even when operating at large signal levels.

(iv) Since the power gain vs. normalized interaction length curves of Figs. 7(a) and 7(b) may be interpreted as frequency-response curves of the power gain for a TWTA (with a fixed interaction length of course) designed for operation around a centre frequency f_c corresponding to the normalized interaction length d_{opt} for a specified value of the peak gain, the flatness of the maximum in the frequency curve of TWTA implies that the TWTA is capable of broadband operation (i.e., with negligible frequency distortion over the essential bandwidth of the input signal) around the centre frequency when the (actual) interaction length is chosen to be $\bar{d} = v_0 d_{opt}/2\pi f_c$.

In addition to the sheath-helix model of the slow-wave structure being incompatible with the actual coupling arrangements employed in a practical TWTA to carry r.f. power into and out of the tube, necessitating the unconventional definitions of power gain and conversion efficiency adopted in this paper, possible reflection of the traveling electromagnetic wave from the collector end has been totally neglected in the present analysis. In view of these shortcomings, the numerical values of the TWTA parameters like power gain, conversion efficiency, optimum interaction length etc., arrived at on the basis of the large-signal field theory presented in Part 1 may not match exactly with those measured experimentally.

The present analysis may be routinely extended to the case of a finite-duration input signal using a Fourier-series representation of the input signal over its time duration. However, if the TWTA has been designed for operation with maximum gain at the fundamental frequency (reciprocal of the signal duration), then the higher harmonics components will get amplified to progressively lower levels resulting in an output signal that has been subjected to severe frequency distortion.

REFERENCES

1. Collin, R. E., *Foundations for Microwave Engineering*, 2nd Edition, IEEE Press, 2005.
2. Kalyanasundaram, N., "Large signal field analysis of an O-type traveling wave amplifier. Part 1: Theory," *IEE Proc. I, Solid-State & Electron Dev.,* Vol. 131, No. 5, 145–152, 1984.
3. Kalyanasundaram, N. and R. Chinnadurai, "Large signal field analysis of an O-type traveling wave amplifier. Part 2: Numerical results," *IEE Proc. I, Solid-State & Electron Dev.*, Vol. 133, No. 4, 163–168, 1986.
4. Rowe, J. E., *Nonlinear Electron-wave Interaction Phenomena,* Academic Press, 1965.
5. Detweiler, H. K. and J. E. Rowe, "Electron dynamics and energy conversion in O-type linear beam devices," *Advances in Microwaves 6*, L. Young, Ed., 29–123, Academic Press, 1971.
6. Hughes Aircraft Company, Electron Dynamics Division, *TWT and TWTA Handbook,* Torrance, California, 1975.
7. Gewartowski, J. W. and H. A. Watson, *Principles of Electron Tubes*, Van Nostrand, 1968.